

## Optical-coherence tomography of a dense tissue: statistics of attenuation and backscattering

To cite this article: J M Schmitt *et al* 1994 *Phys. Med. Biol.* **39** 1705

View the [article online](#) for updates and enhancements.

### You may also like

- [Ising ferrimagnetic models. I](#)  
G M Bell
- [Superexchange in manganese formate dihydrate, studied by polarized-neutron diffraction](#)  
P Radhakrishna, B Gillon and G Chevrier
- [Existence of phase transitions in a model three-component solution](#)  
D A Huckaby, J M Kowalski and M Shinmi

**JOIN US | ESTRO 2024**

**In-Booth Talks, Demos,  
& Lunch Symposium**

[Browse talk schedule >](#)



## Optical-coherence tomography of a dense tissue: statistics of attenuation and backscattering

J M Schmitt†, A Knüttel‡, M Yadlowsky† and M A Eckhaus§

† Biomedical Engineering and Instrumentation Program, NCRR, National Institutes of Health, Bethesda, MD 20892, USA

‡ Laboratory of Cellular Biology, NHLBI, National Institutes of Health, Bethesda, MD 20892, USA

§ Veterinary Resources Program, NCRR, National Institutes of Health, Bethesda, MD 20892, USA

Received 18 April 1994, in final form 28 June 1994

**Abstract.** This paper addresses fundamental issues that underlie the interpretation of images acquired from turbid tissues by optical-coherence tomography (OCT). The attenuation and backscattering properties of freshly excised rat arteries and their dependence on the focusing and collection optics of the OCT system were measured at two wavelengths in the near infrared (830 nm and 1300 nm). Determined from the ratio of the magnitudes of the reflections from glass plates placed on both sides of the arteries, the mean attenuation coefficient of the arterial wall was found to be in the range  $14 < \mu_t < 22 \text{ mm}^{-1}$  at 830 nm and  $11 < \mu_t < 20 \text{ mm}^{-1}$  at 1300 nm. The measured values of  $\mu_t$  were lowest for the longer source wavelength and for probe beams with the smallest average diameters. The observed dependence of  $\mu_t$  on beam size indicates that relatively large-scale variations in the index of refraction of the tissue contributed to degradation of the transverse spatial coherence of the beam. We introduce a framework for understanding and quantifying beam-size effects by way of the mutual-coherence function. The fact that spatial variations in backscattering and attenuation (which includes spatial-coherence losses) have similar effects on OCT signals makes the origin of the signals difficult to determine. Evidence is given that suggests that, in spite of this difficulty, certain features of microstructures embedded several hundred micrometres deep in a turbid tissue can still be detected and characterized.

### 1. Introduction

Optical-coherence tomography (OCT) has undergone rapid development since its first application to imaging of microstructures in the eye (Fercher *et al* 1988, Hitzengerber 1991, Swanson *et al* 1994, Huang *et al* 1991). In most of the earliest studies, efforts were concentrated on recording specular reflections from nearly transparent structures. Our group and others have recently begun to investigate techniques for measuring local properties of skin, blood vessels, and other optically turbid tissues *in vivo* with OCT (Huang *et al* 1991, Clivaz *et al* 1992, Schmitt *et al* 1993a–c). In these tissues, optical attenuation is higher, backscattering is weaker, and reflections are poorly defined; moreover, multiple scattering and speckle complicate the interpretation of the OCT signals.

The OCT image of the nail fold region of the finger in figure 1 illustrates some of these problems. This image was obtained from living tissue with a fibre-optic OCT scanner configured similarly to that described by Huang *et al* (1991). Knowing the anatomy of the skin in this region, one can identify the nail, cuticle, papillary dermis, and other structures

in the image based on their shapes. Note, however, that no clear relationship exists among the magnitudes of the reflected signal powers measured from the various regions, which, in this example, cover a range of nearly 60 dB. Why, for example, do the reflections from the nail, which appear uniformly strong over most of the cross section of the nail body (see the far left of figure 1), suddenly vanish where the nail enters the cuticle skin fold? Why do the OCT signals measured from the dermis appear stronger than those measured from the overlying epidermis? To answer these and other related questions, the mechanisms by which the OCT probe beam is attenuated and backscattered by soft tissue need to be better understood. It is also important to understand the extent of the intrinsic variation that exists in the optical properties of biological tissues as measured by OCT on a microscopic scale, and how these properties depend on wavelength.

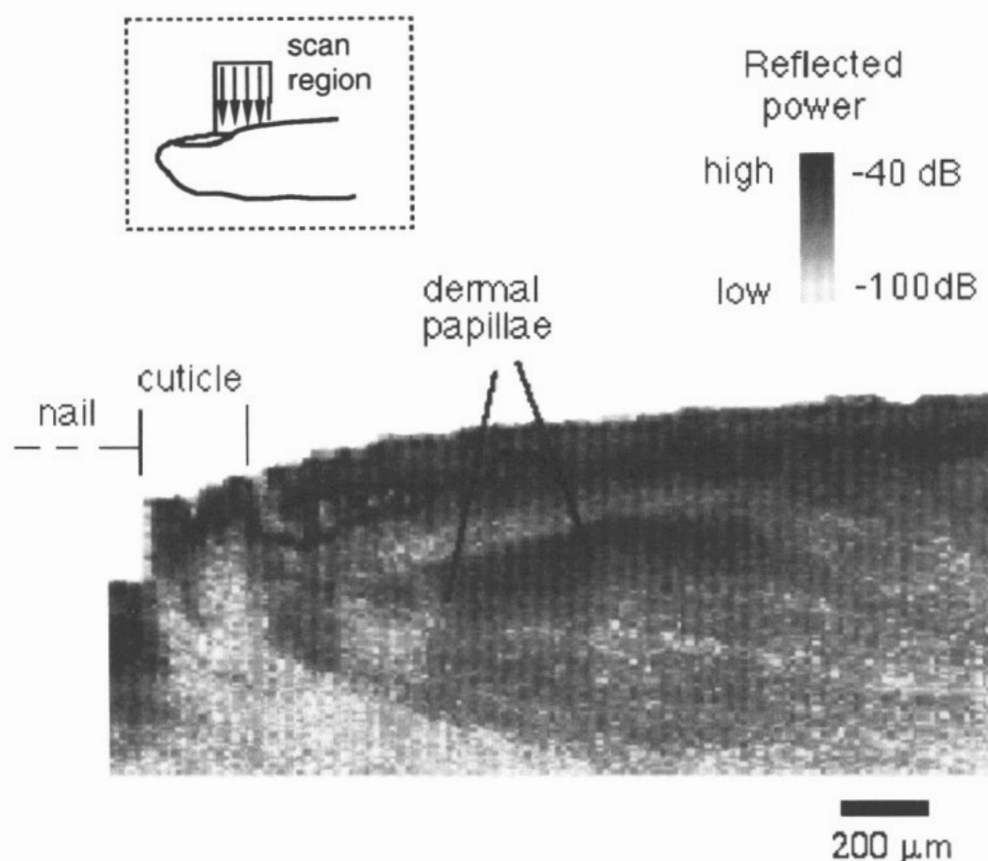


**Figure 1.** Cross-sectional image of a region of the index finger in the vicinity of the nail fold acquired with a fibre-optic OCT scanner (LED wavelength = 1300 nm). Inset: a diagram showing the orientation of the scan lines along which the light was collected with the sample fibre. The light from the sample fibre was collimated with a 38 mm focal-length lens and focused on the tissue with a scanning 10 $\times$  objective, which also captured the backscattered light from the tissue. The scale in the upper right relates the image grey level to the reflected signal power, measured in decibels below that produced by a perfectly reflecting target.

This paper addresses these basic issues. From measurements made *in vitro*, we distinguish the effects of attenuation and backscattering on OCT of freshly excised rat arteries at two wavelengths in the near infrared (830 nm and 1300 nm) and their dependence on focusing of the probe beam. These results permit us to make general statements about OCT imaging of heterogeneous soft tissues. The statistical variability of the backscattering and attenuation coefficients of the arteries are shown to depend on the beam focusing and collection optics of the OCT system, as well as the intrinsic heterogeneity of the tissue. Knowledge of these properties is essential for evaluating the feasibility of imaging vascular tissue with OCT and for developing new techniques for extracting clinically relevant information from optical-coherence tomograms of other turbid tissues. Our results suggest that the single-backscattering model (Schmitt *et al* 1993a,b), although adequate for characterizing the average optical properties of a turbid tissue, does not account for the effects of multiple scattering, which can play an important role in OCT. To properly interpret the signals recorded by an OCT system, one must understand the effects of both large- and small-scale variations in the indices of refraction of tissues on the loss of spatial coherence of the probe beam. This paper introduces a framework for understanding and quantifying these effects by way of the mutual-coherence function. The major implication of this study is that an OCT system, particularly its focusing and collection optics, needs to be designed with knowledge of the type of information that one wishes to accentuate in the processed images.

## 2. Materials and methods

### 2.1. Apparatus

Optical-coherence tomograms were obtained with the low-coherence interferometry system shown in figure 2. The configuration of the system was similar to that used in earlier studies

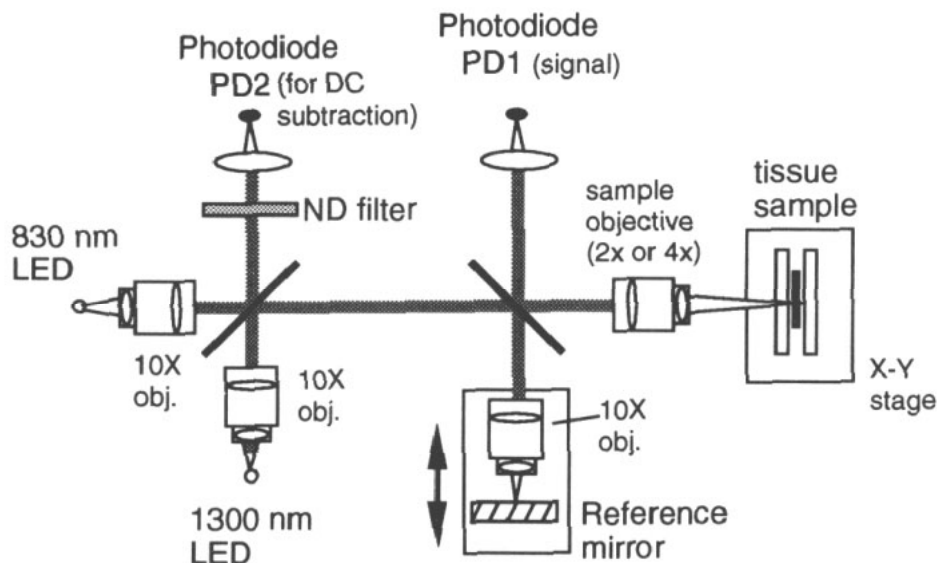


**Figure 2.** The optical layout of the OCT system built in our laboratory to carry out measurements on excised biological tissues. The operation of the system is explained in section 2.1 of the text.

(Schmitt *et al* 1993c), except that in the present study two light sources, superluminescent LEDs with peak emissions at 830 nm (Model L3302, Hamamatsu Corp.) and 1300 nm (OE303S, OKI Corp.), were employed instead of a single light source. This allowed us to rapidly record scans at both wavelengths by switching between the sources. The signal-detection photodiode (PD1) and an additional photodiode (PD2) that served as a light-source monitor for DC light subtraction were both fabricated from InGaAs, which has a spectral response that covers the emission wavelengths of the two sources. A mirror on a translation stage was moved at a constant velocity over the measurement range to vary the length of the optical path in the reference arm and simultaneously modulate the frequency of the interference signal. For the velocity at which the stage was moved ( $3.5 \text{ mm s}^{-1}$ ), the modulation was centred on Doppler-shift frequencies of 8.4 kHz and 5.3 kHz, respectively, for the 830 nm and 1300 nm sources. The magnitude of the interference signal at each wavelength was recorded as a function of mirror position by filtering the preamplified signal from PD1 within a 2 kHz passband centred on its respective Doppler-shift frequency and measuring the RMS power of the resultant signal. Set by the apertures of  $10\times$  objectives that collected light from the LEDs, the diameters of the collimated beams were both equal to about 7 mm.

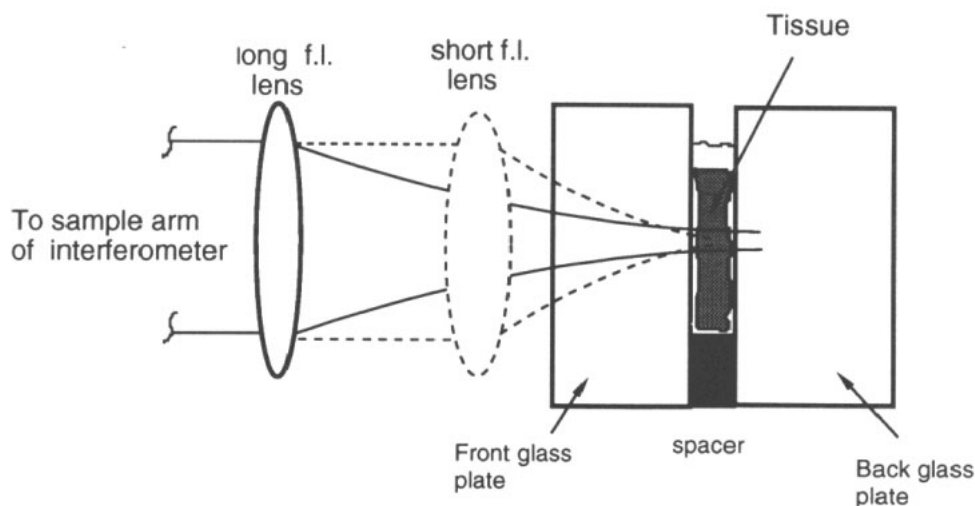


**Figure 3.** A close-up of the chamber used to hold the specimens.

Figure 3 shows an expanded view of the chamber in which the excised tissue specimens were placed. The specimen under measurement was held tightly in the space between two glass plates which was filled with phosphate-buffered saline. Besides holding the specimen, the glass plates also served as reference surfaces for the measurement of attenuation through the tissue. The ratio between the reflections at the front and back glass–tissue interfaces was used to quantify the coherence losses in the tissue resulting from both scattering and wavefront distortion. To ensure that the strong reflections from the glass–air interfaces did not interfere with the measurement, glass plates with thicknesses at least 10 times the temporal coherence lengths of the sources were used. The source beams were either focused to a minimum at the centre of the sample chamber or at the surface of the back glass plate. Because the optical components in the system had different optical properties within the

wavelength bands of the two sources, the positions of the minimum beam waist in the sample and the distances from the sample objective at which the optical pathlengths in the reference and source arms matched differed slightly at the two wavelengths.

To examine the effects of the focal beam-spot diameter on attenuation and backscattering, the experiments were carried out using either a 4× objective (focal length = 30 mm) or a 2× objective (focal length = 45 mm) to focus the source beam on the sample. Estimated from measurements made with the sample chamber filled with water assuming Gaussian beam optics, the minimum beam diameter,  $d_{\min}$ , and Rayleigh range,  $z_R = \pi d_{\min}^2 / 4\lambda$ , of the focused beam for the different sources were as follows:  $d_{\min} = 8 \mu\text{m}$ ,  $z_R = 60 \mu\text{m}$  (4× objective at 830 nm);  $d_{\min} = 12 \mu\text{m}$ ,  $z_R = 90 \mu\text{m}$  (4× objective at 1300 nm);  $d_{\min} = 10 \mu\text{m}$ ,  $z_R = 90 \mu\text{m}$  (2× objective at 830 nm); and  $d_{\min} = 17 \mu\text{m}$ ,  $z_R = 180 \mu\text{m}$  (2× objective at 1300 nm).

## 2.2. Tissues

Arterial tissues were obtained from rats shortly after they were sacrificed for an animal-health survey conducted by the Veterinary Research Program at the National Institutes of Health. Upon removal, a short segment of the aorta of each rat was cut open and laid flat to expose its lumen. The periadventitial adipose tissue was scraped away to reduce the thickness of the specimen for the transmission measurements. The specimen was then cut into several square pieces (3 mm × 3 mm). One of the pieces was fixed in formalin for later histology and the remaining pieces were placed between gauze pads soaked in phosphate-buffered saline for transport to the laboratory. Measurements were made within 1 h after sacrifice.

## 2.3. Measurement procedure

Before placing a specimen in the sample chamber, we adjusted the focus of the objective lens by measuring the relative magnitudes of the reflections from the front and back glass-water interfaces of the chamber filled with water. The specimen was then placed in the chamber with its intimal surface facing the incident beam. With the tissue held stationary, five depth scans were taken in rapid sequence and the averaged depth profile for that position was recorded. The tissue was then translated perpendicular to the longitudinal axis of the (uncut) artery and five more scans were taken and averaged. This process was repeated until the desired number of scans was completed.

## 2.4. Data analysis methods

As in earlier studies (Schmitt *et al* 1993a, b), we analysed the results of the present study by assuming that the backscattered signal power measured by the interferometer in a single scan can be described by a simple exponential relationship,

$$P(z') \simeq P_i A(z') L_c \mu_b \exp(-2\mu_t z') \quad (1)$$

where  $P_i$  is the incident power in the sample beam,  $z'$  is the translation distance of the reference mirror,  $A(z')$  is the aperture function of the interferometer,  $L_c$  is the temporal coherence length of the source, and  $\mu_b$  and  $\mu_t$  are the volumetric backscattering coefficient ( $\text{mm}^{-1} \text{sr}^{-1}$ ) and total attenuation coefficient ( $\text{mm}^{-1}$ ), respectively, of the tissue. Over the depths probed in these experiments, absorptive losses were negligible compared to scattering losses, so that  $\mu_t \simeq \mu_s$ , where  $\mu_s$  is the scattering coefficient or reciprocal mean-free path. Measured in air,  $z'$  corresponds to depth  $z = z'/n_s$  in the tissue, where  $n_s$  is the tissues

bulk index of refraction (assumed equal to 1.38 for the tissues measured in this study). The function  $A(z')$  represents the effective field of view of the receiver, which depends on the focusing and collection optics of the interferometer. It can be viewed as the aperture over which efficient mixing with the reference beam occurs. In this study, since the backscattered power was measured relative to the reflection from the glass walls of the sample chamber, we only needed to account for the change in  $P(z')$  within the measurement zone that resulted from focusing by the objective lens in the sample arm. We assumed that the beam in the interferometer had a Gaussian intensity profile, so that the relative change in  $P(z')$  for reflection from a glass plate could be written as  $P_g(z')/P_g(z'_{\min}) = \{1 + [(z' - z'_{\min})/z_R]^2\}^{-1/2}$ , where  $P_g(z'_{\min})$  is the signal power measured with the glass-water interface in the focal plane of the objective lens (where the beam waist is minimum) and  $z_R$  is the Rayleigh range of the focused beam (estimated values for  $z_R$  for the objective lenses used in the experiments are given in section 2.1). Using the measured values of  $P_g(z'_{\min})$ ,  $z'_{\min}$ , and  $z_R$ , we calculated the fraction of the coherent optical power backscattered from the tissue relative to a perfect reflector according to

$$P_{\text{rel}}(z') = P(z')R_g/P_g(z') \quad (2)$$

where  $R_g$  is the reflection coefficient of the glass wall of the chamber (index of refraction,  $n_g = 1.5$ ) in contact with water (index of refraction,  $n_w = 1.33$ ), which is given by  $[(n_g - n_w)/(n_g + n_w)]^2 \approx 0.36$ . The quantity  $P_{\text{rel}}(z')$ , calculated according to equation (2), represents the (dimensionless) backscattered power-against-depth profile corrected for focusing by the objective lens.

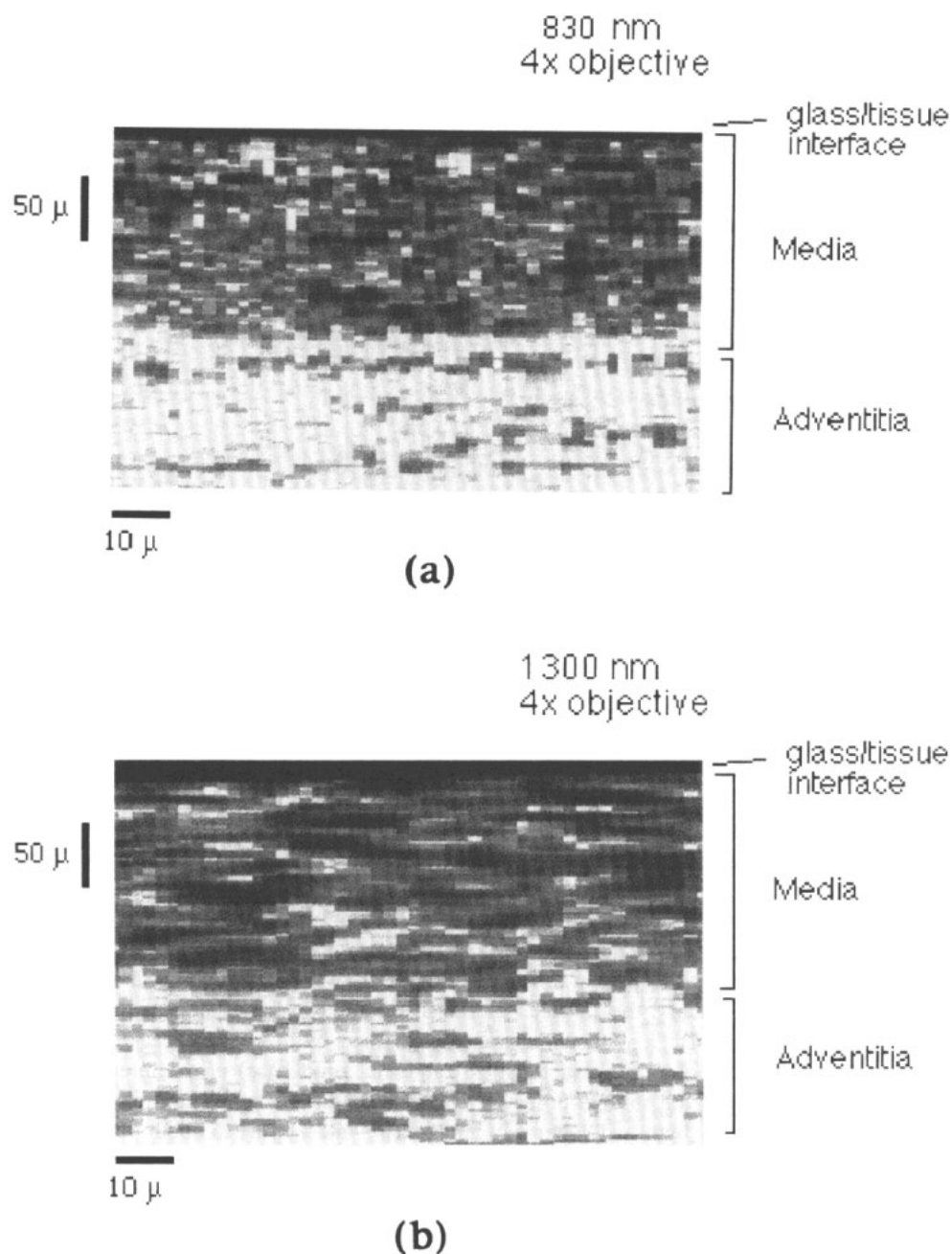
The mean attenuation coefficient,  $\mu_t$ , measured along the path of the beam was calculated from the ratio  $R$  between the signal powers generated by reflections from the front and back tissue-glass interfaces, according to  $\mu_t = \ln R/(2L_t)$ , where  $L_t$  is the thickness of the tissue. To calculate the average power backscattered by the tissue, we multiplied the  $P_{\text{rel}}(z')$  values by  $\exp[\mu_t(z'/n_s)]$  to compensate for the mean attenuation and averaged the resultant quantity over the entire thickness of the tissue.

### 3. Results

Optical-coherence tomograms of the backscattered power measured within a two-dimensional region of the rat artery are shown in figure 4. The tomograms were synthesized from depth profiles measured at the two source wavelengths (830 nm and 1300 nm), for a lateral step size equal to 1  $\mu\text{m}$ . The measured values of  $P_{\text{rel}}(z')$  were first corrected for mean attenuation as discussed in section 2.4 and then converted to logarithmic values for display on a grey scale. For comparison, figure 5 shows a photomicrograph of an adjacent segment of the same artery stained with haematoxylin and eosin dyes.

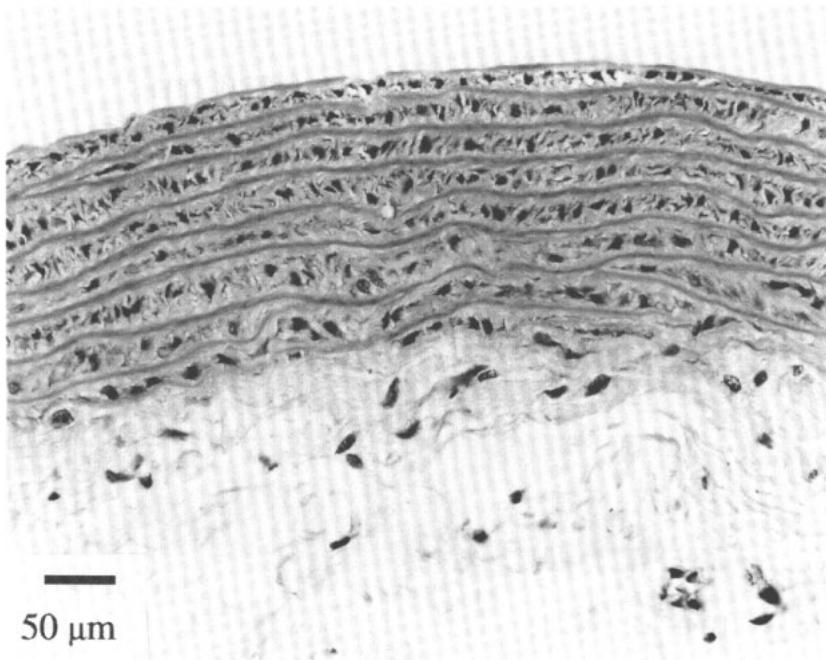
In spite of the relatively coarse focusing provided by the 4 $\times$  objective, significant variations in the backscattered power were seen on the 1  $\mu\text{m}$  scale at both wavelengths. Most of these variations, however, appear to be random and only correspond grossly to the structure evident in figure 5. At both wavelengths, the media and adventitia are differentiated quite clearly, but the cellular structures within the media are not. In the 1300 nm tomogram, highly reflecting regions running parallel to the intimal surface of the artery are evident which may correspond to the bands of elastin fibres in the media; these regions, however, are absent from the 830 nm tomogram.

Figure 6 shows depth profiles extracted from the 830 nm and 1300 nm tomograms. Although the profiles were obtained from the same lateral position on the artery, the



**Figure 4.** Optical-coherence tomograms recorded from a rat artery with the laboratory OCT system: (a) source wavelength = 830 nm; (b) source wavelength = 1300 nm. The intimal side of the artery was in contact with the front glass plate.





**Figure 5.** A section of a rat artery ( $\sim 6\ \mu\text{m}$  thick) stained with haematoxylin and eosin dyes. The upper surface is the intima of the artery.

positions and magnitudes of the reflections show only a weak correlation between the two wavelengths. Note that the reflections measured at 830 nm close to the surface tend to merge and have a greater magnitude compared to those measured at 1300 nm. Also note that the attenuation of the backscattered power through the artery, as indicated by the ratio of the front and back glass reflections, is about 15 dB greater at 830 nm than at 1300 nm in this example.

The lack of contrast in the optical-coherence tomograms between adjacent cellular structures can be explained, in the most part, by the averaging effect of the relatively large sample volume of the interferometer. In the ideal case of a tenuous medium in which only single backscattering occurs, the sample volume in the focal plane of the objective would be approximately cylindrical, with dimensions determined by the coherence length of the source and the directional gain characteristics ('antenna' properties) of the interferometric detector transformed by the sample objective (Siegman 1966). The 830 nm and 1300 nm superluminescent diodes both had coherence lengths (in water) equal to about  $15\ \mu\text{m}$  at the current levels (100 mA) used in this study. This length exceeded the widths of many of the cell layers in the arterial sample. Because the antenna properties of an interferometric receiver depend on wavelength for a given reference beam size, the lateral dimension of the sample volume—again, assuming the ideal case of a single-scattering medium—would be expected to be smaller at 830 nm than at 1300 nm by a factor of  $1300/830 \approx 1.6$  (Siegman 1966). The smaller effective sample volume may partly explain the blotchier appearance of the 830 nm tomogram compared to that of the 1300 nm tomogram.

Arguments based on a single-scattering model of tissue, however, are not sufficient to entirely explain the behaviour of the spatial variations in attenuation and backscattering

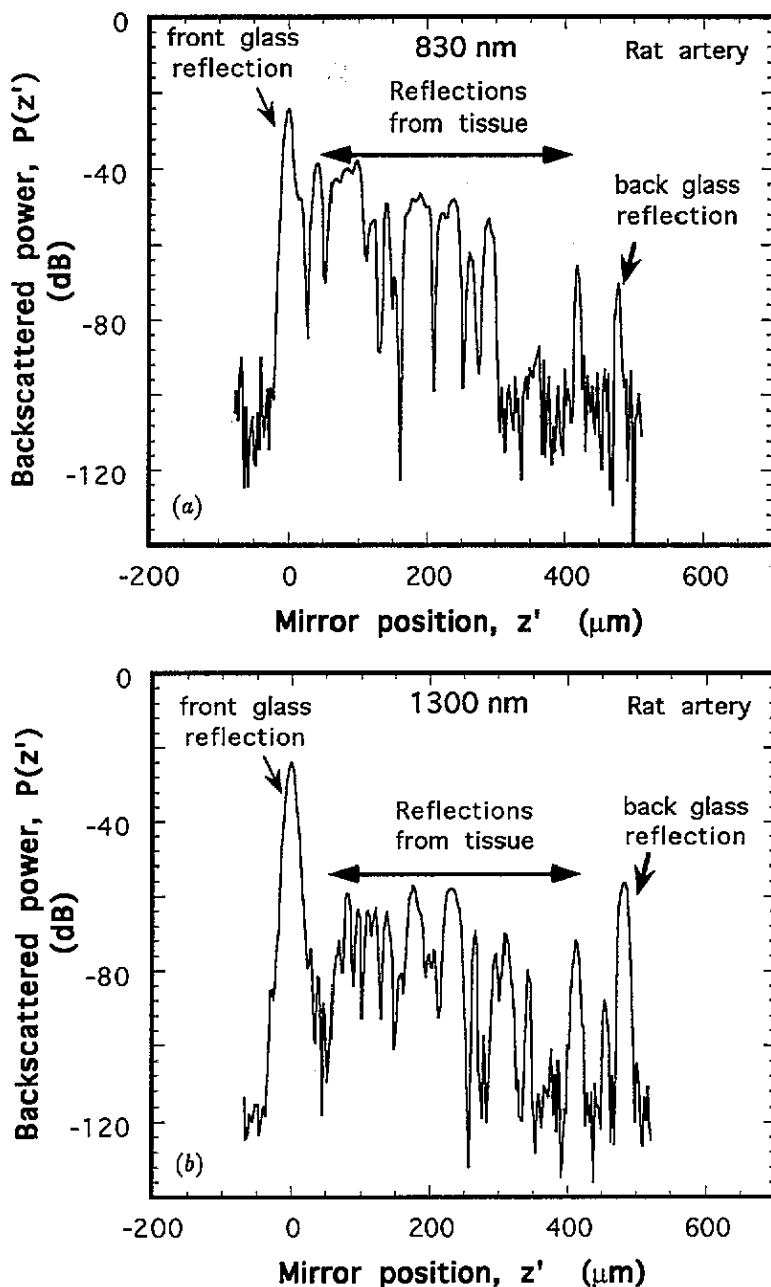


**Figure 6.** Examples of depth profiles recorded from a rat artery with the laboratory OCT system: (a) source wavelength = 830 nm; (b) source wavelength = 1300 nm. The intimal side of the artery was in contact with the front glass plate.

observed in our experiments. This can be seen from the data displayed in figure 7, which shows histograms of the attenuation coefficient ( $\mu_t$ ) measured for different lateral positions of the sample beam along a rat artery. Data obtained under two different focusing conditions

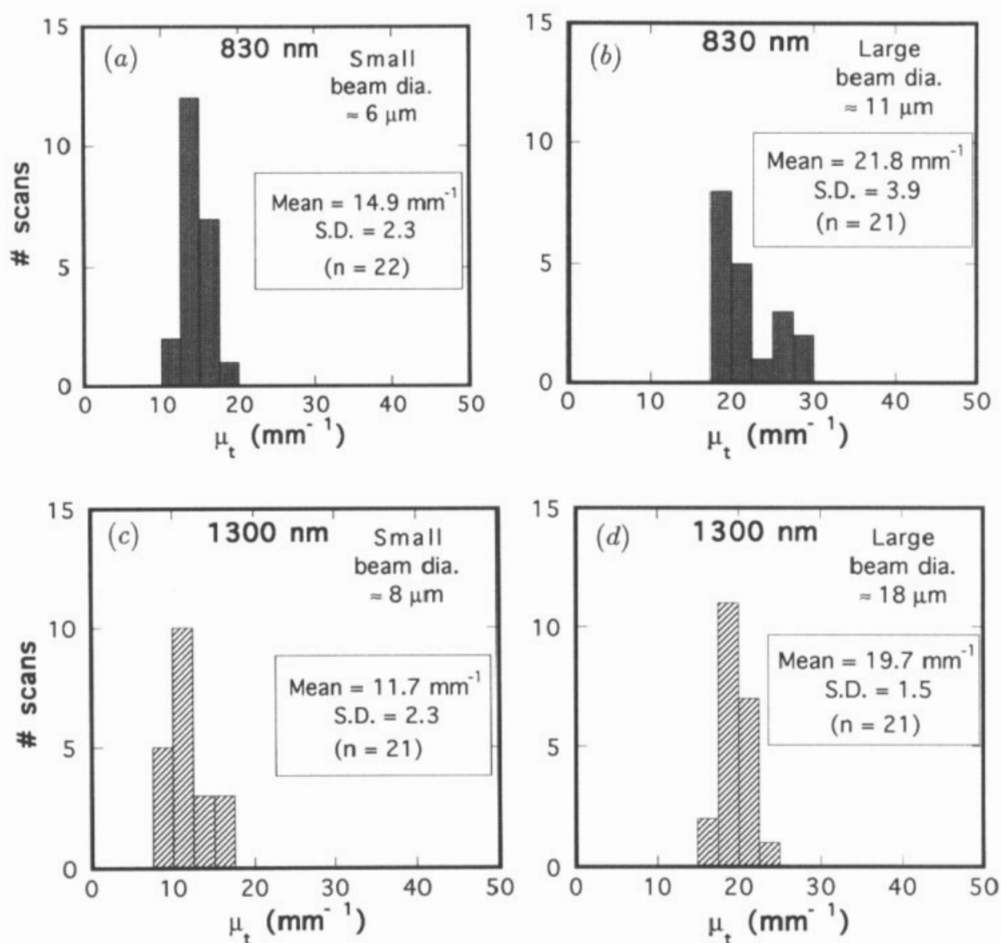


**Figure 7.** Histograms of the mean attenuation coefficient measured at different lateral positions on a rat artery: (a) 830 nm, 4 $\times$  objective focused midway between the front and back glass plates; (b) 830 nm, 2 $\times$  objective focused on the back glass plate; (c) 1300 nm, 4 $\times$  objective focused midway between the front and back glass plates; and (d) 1300 nm, 4 $\times$  objective focused on the back glass plate. The measured focal-spot sizes averaged over the thickness of the artery are given in the upper right-hand corner of each plot.

are shown. The histograms labelled 'small beam diameter' show the distributions measured with the beam focused in the middle of the arterial sample and the curves labelled 'large beam diameter' show the distributions measured with the beam focused on the far wall of the arterial specimen. Data are shown for both the 1300 nm and 830 nm sources. The objective lenses used in the experiments (see the caption of figure 7) were chosen to make the diameter of the beam averaged over the entire thickness of the specimen in the small-diameter case smaller by a factor of about two at both wavelengths than in the large-diameter case ( $6 \mu\text{m}$  versus  $11 \mu\text{m}$  at 830 nm;  $8 \mu\text{m}$  versus  $18 \mu\text{m}$  at 1300 nm).

These results demonstrate that the beam-coherence losses through the arterial specimens, as measured by the reflectivity of a flat glass plate placed behind the specimens, depend

strongly on wavelength and on the width of the probe beam. The effects of these variables on beam coherence have been recognized by others in previous studies of beam propagation in a turbulent atmosphere (Yura 1974, Kazovsky and Kopeika 1983). In the experiments in which the average diameters of the beams at the two source wavelengths were nearly equal, the signal attenuation was found to be considerably less, on average, for the 1300 nm source compared to the 830 nm source. For example, as shown by comparing figures 7(a) and (c), the mean value of  $\mu_t$  measured at 1300 nm was more than 20% less than that measured at 830 nm ( $11.7 \text{ mm}^{-1}$  versus  $14.9 \text{ mm}^{-1}$ ), even though the average beam diameter at 1300 nm was slightly larger ( $8 \text{ }\mu\text{m}$  versus  $6 \text{ }\mu\text{m}$ ). In their round-trip passage through the tissues, the small-diameter beams were attenuated significantly less than the large-diameter beams at both wavelengths: at 830 nm, the mean value of  $\mu_t$  increased from  $14.9 \text{ mm}^{-1}$  to  $21.8 \text{ mm}^{-1}$  with beam diameter; at 1300 nm,  $\mu_t$  increased from  $11.7 \text{ mm}^{-1}$  to  $19.7 \text{ mm}^{-1}$ .

The relationship between the backscattered signal power ( $P_{\text{rel}}$ , from equation (2), averaged over the entire thickness of the artery) and  $\mu_t$  at different lateral positions is plotted in figure 8. The two variables showed a weak linear correlation at both wavelengths with a slope that exhibited no statistically significant dependence on either wavelength or the average diameter of the probe beam. At 1300 nm, the signal power measured with the large-diameter beam increased substantially compared to the signal power measured with the small-diameter beam. This increase, which is consistent with that expected for a beam backscattered from a larger volume of independent scatterers, was not observed at 830 nm. As indicated by equation (1), local variations in  $\mu_b$  or  $\mu_t$  can both cause a change in the magnitude of the signal power measured at a given optical depth  $z'$ . To separate the effects of  $\mu_b$  and  $\mu_t$  variations, some functional relationship between these variables must be assumed or measured (Parameswaran *et al* 1991). These data suggest that this relationship for a given tissue type can only be specified as a spatial average, because of the inhomogeneity of the indices of refraction, sizes, and shapes of the cellular structures in the tissue.

Figure 9 shows an example of a depth profile (lower curve) that was calculated by averaging 20 depth scans taken at lateral positions separated by  $20 \text{ }\mu\text{m}$ . The curve in the figure labelled 'attenuation corrected' (upper curve), which was obtained by multiplying the averaged profile by  $\exp[\mu_t(z'/n_s)]$ , represents the depth dependence of  $\mu_b$  averaged over a  $400 \text{ }\mu\text{m}$  wide cross-section of the artery. Note that the transition between the media and the adventitia of the artery is discernible in the attenuation-corrected curve by a decrease in backscattered signal power at  $z' \simeq 300 \text{ }\mu\text{m}$ .

In the next section (section 4) we discuss the preceding experimental observations in the context of the theory of partially coherent wave propagation in a random medium.

#### 4. Discussion

A beam of light progressively loses spatial coherence as it penetrates deeper in a turbid biological tissue. In most soft tissues of the body, this loss of coherence results from scattering by a variety of cellular structures with sizes ranging from less than a wavelength (e.g., cellular organelles) to several hundreds of micrometres (e.g., the length of a collagen fibre).

As illustrated in figure 10, the dominant scattering interactions of a light beam propagating in a turbid tissue can be categorized into three types: (i) single backscatter, (ii) extinction by absorption or wide-angle scatter (i.e. light scattered out of the path of the beam and out of the field of view of the interferometric receiver), and (iii) small-angle forward scatter, which is taken here to include scattering by discrete scatterers and by

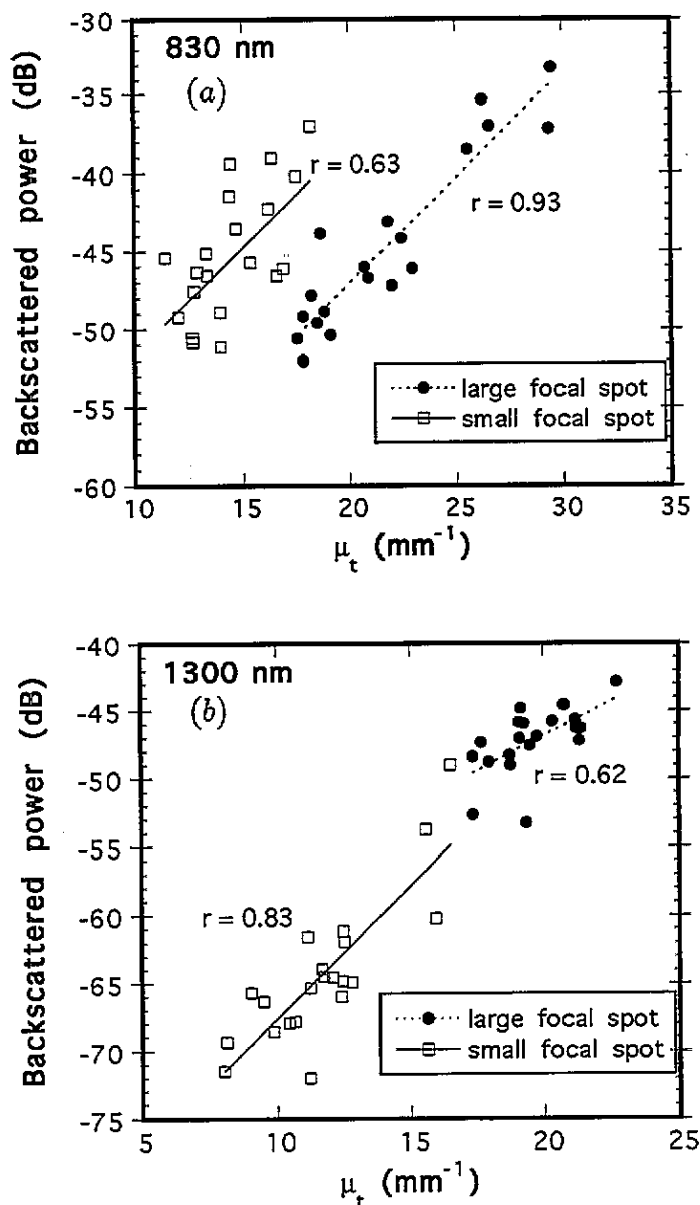
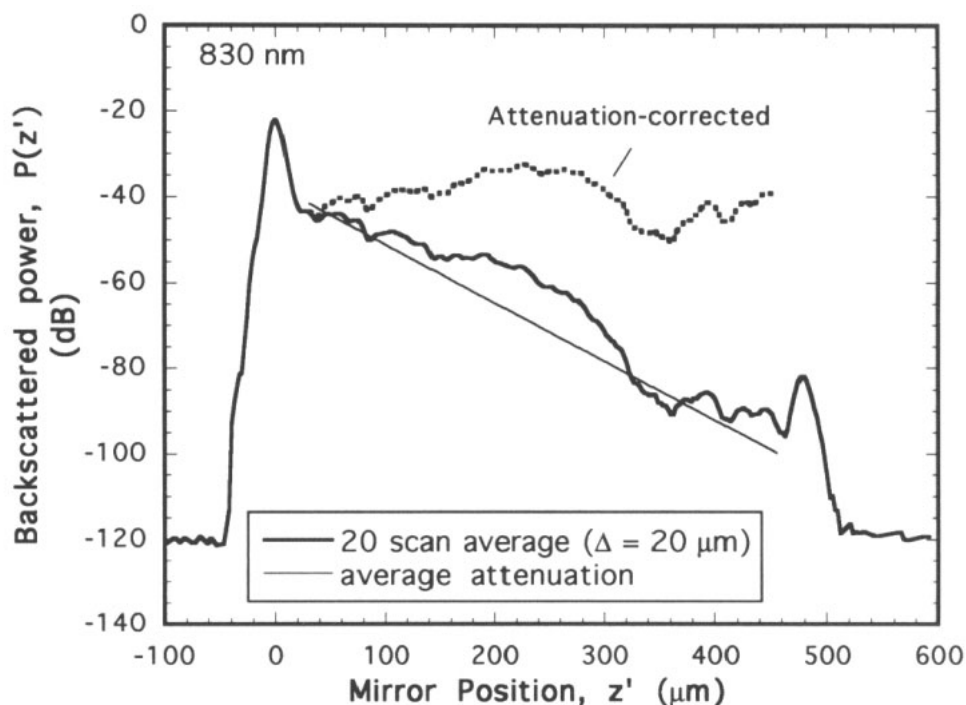


Figure 8. The correlation between backscattered power and mean attenuation measured at various lateral positions on a rat artery with a probe beam having two different focal-spot sizes: (a) source wavelength = 830 nm and (b) source wavelength = 1300 nm.

continuous, large-scale variations in the local index of refraction, analogous to the refractive inhomogeneities caused by atmospheric turbulence. The single-backscatter model, which has been applied in the measurement of the optical properties of tissues by low-coherence reflectometry (Schmitt *et al* 1993a, b) and in the analysis of atmospheric lidar data (Anderson and Browell 1972), explicitly incorporates scattering interactions of types (i) and (ii) only. In view of the dependence of the effective extinction and backscattering coefficients of tissue on beam size observed in this study, the single-backscattering model appears to give



**Figure 9.** The average of depth profiles recorded at 20 adjacent positions (lateral separation = 20  $\mu\text{m}$ ) on a rat artery (830 nm source wavelength). The curve labelled 'attenuation corrected' shows the profile that resulted from correcting the average profile for the measured loss in coherence with depth in the tissue.

an incomplete description of coherent beam propagation in tissues. While the extinction coefficient or mean free path can be used to characterize the loss of light from the beam for roughly calculating quantities of interest such as the maximum probing depth of OCT, a more general model is needed to describe how design parameters of an OCT system influence its performance when imaging a tissue containing structures with a wide range of dimensions.

To gain insight into how the different scattering interactions affect the signals acquired by an OCT system, it is useful to introduce the concept of the mutual-coherence function (MCF), which is defined as  $M(r_1, r_2) \equiv \langle U(r_1)U^*(r_2) \rangle$ , where  $U(r_1)$  and  $U(r_2)$  are the electric fields at two points,  $r_1$  and  $r_2$ , in a plane perpendicular to the axis of a propagating beam (Born and Wolf 1983). From this definition, it can be seen that the MCF describes the transverse spatial coherence of the beam. If the MCFs of the reference beam,  $M_r$ , and of backscattered light returning from the tissue,  $M_t$ , are known, then the magnitude of the signal power produced when the beams are mixed at the detector of an interferometer can be calculated as follows (Yura 1979):

$$\langle i_s^2 \rangle \propto \int_{\text{detector}} \int M_r(r_1, r_2) M_t(r_1, r_2) d^2 r_1 d^2 r_2 \quad (3)$$

where the integration is taken over the area of the detector and the angle brackets denote an ensemble average taken over the measurement period. Note that the time dependence of  $M_r$  and  $M_t$  is not included explicitly in equation (3). We assume here that the mean optical

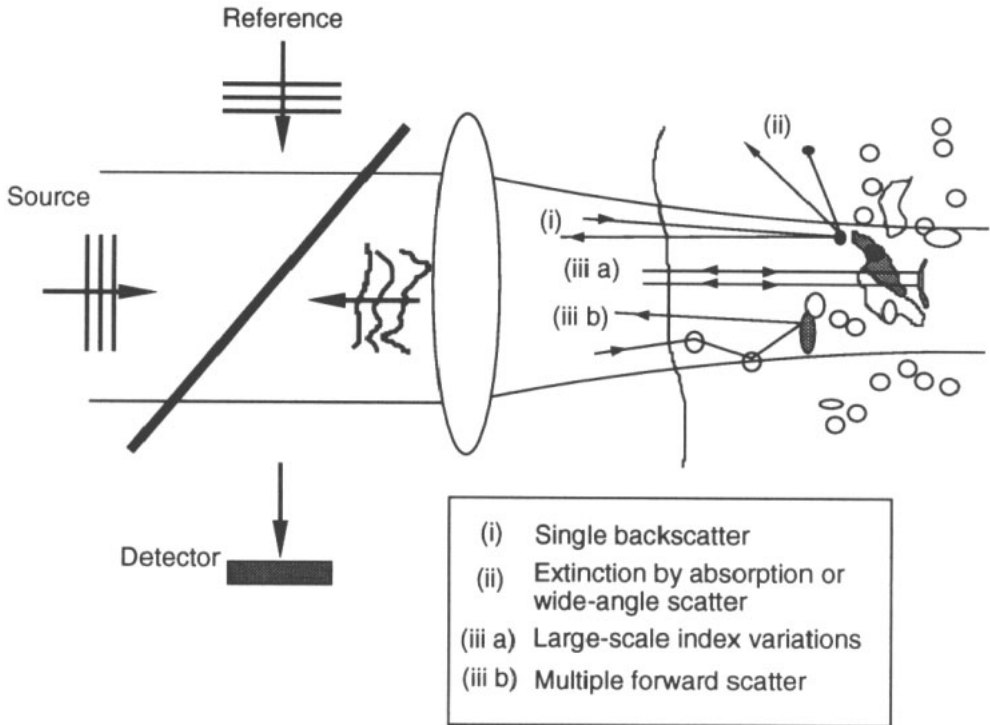


**Figure 10.** Scattering interactions between a beam and structures in a turbid tissue. The three main types of interaction (i)–(iii) illustrated in the figure are discussed in the text.

pathlength between the detector and the plane of interest in the tissue is the same as that between the detector and the reference mirror. In the Michelson interferometer used in this study, the MCF of the reference beam can be approximated as a plane wave of finite extent which effectively sets the detection area over which  $M_t$  is integrated. Therefore, the mixing efficiency depends directly on the mutual coherence of the light backscattered from the tissue that strikes the detector within the area defined by the cross section of the reference beam. By backpropagating the reference beam (Siegman 1966), the effective detector plane can be moved to any plane convenient for evaluation of equation (3).

The effects of the different scattering interactions depicted in figure 10 can be conveniently represented as a product of MCFs that comprises separate MCFs associated with the different types of scattering interaction (Lutomirski 1978)

$$M_t = M_0 M_{\text{ext}} M_{\text{fwd}}. \quad (4)$$

Here  $M_0$  is the MCF of the unscattered focused beam.  $M_{\text{ext}}$  is the MCF calculated by neglecting all scattering interactions except those interactions that absorb light or scatter it completely out of the field of view of the interferometric receiver (the type-(ii) interactions illustrated in figure 10). Independent of the lateral extent of the beam,  $M_{\text{ext}}$  simply represents an exponential loss in the amplitude of the unscattered component of the probe beam as it propagates deeper in the medium. This loss results from interaction of the beam with randomly positioned molecules or other scatterers with sizes much smaller than the source

wavelength and can be described by the transport theory for specific intensity in a particulate medium. In the context of transport theory, the isotropic scattering coefficient accounts for these losses (Ishimaru 1978). On the other hand,  $M_{\text{fwd}}$  is associated with scattering interactions of type (iii) that do not necessarily scatter light completely out of the path of the beam but still decorrelate the optical field, an effect that is difficult to describe explicitly using conventional transport theory.

With these definitions and observations in mind, we can now consider in greater detail the experiments in this study in which specular reflection from a flat glass plate placed behind a tissue specimen was used to measure the attenuation and decorrelation of the incident beam by the tissue. The MCF of the optical field reflected by a structure that is flat on the scale of the beam diameter is proportional to the MCF of the incident field,  $M_0$ . With a slab of tissue interposed, the scattering interactions that the beam undergoes during its double passage through the tissue alter the MCF of the reflected field in proportion to the quantity  $M_{\text{ext}}M_{\text{fwd}}$ . As defined, the wide-angle scattering interactions described by  $M_{\text{ext}}$  only reduce the amplitude of the forward-propagating coherent field, without changing the form of  $M_0$ . On the other hand, the forward-scattering interactions described by  $M_{\text{fwd}}$  produce scattered fields that interfere with the incident field and alter its MCF. The result is that speckle spots, which have a characteristic coherence length that depends on the density and size of the refractive index variations, form on the detector†.

It is important to realize that the field backscattered by small, randomly distributed particles with dimensions  $l_s \ll \lambda$ , unlike that reflected from a large planar structure like a glass plate, is not sensitive to the beam-size-related degradation in coherence emphasized in this study. This can be seen by noting that the MCF of a field backscattered by such particles is approximately given by (Yura 1979)

$$M_{\text{pt}}(r_1, r_2) = \delta_2(r_1 - r_2)U(r_1, r_1) = \delta_2(r_1 - r_2)\langle I_0(r_1) \rangle \quad (5)$$

where  $\langle I_0(r_1) \rangle$  is the average intensity incident on a particle at point  $r_1$  and  $\delta_2$  is the two-dimensional Dirac delta function. Equation (5) states that  $M_{\text{pt}}$  only depends on the average intensity of the incident field, given by its MCF at zero spacing,  $r_1 - r_2 = 0$ . In the more general case, the MCF of the backscattered field reflects that of the incident field for  $|r_1 - r_2| \leq l_s$ .

The greater apparent attenuation observed in those experiments in which a large-diameter probe beam was used can now be explained by noting that  $M_0$  for such a beam is broader and encompasses a wider range of refractive-structure scale sizes. This leads to a reduction in the effective correlation length of the field incident on the detector, which, in turn, reduces the efficiency with which the field mixes with the reference beam. In effect, a wide beam is susceptible to coherence degradation by structures larger than those that can be 'seen' by a narrower beam. The sizes of a structure relative to the source wavelength determines the degree to which the coherence degradation of the beam affects the mixing efficiency. This dependence of mixing efficiency on wavelength is apparent in the experimental results shown in figure 8. The weak correlation between the effective backscattering coefficient,  $\mu_b$ , and the extinction coefficient,  $\mu_t$ , found in this study (see figure 8) is consistent with the view that the refractive structures that cause loss of spatial coherence of the forward-propagating beam may have different dimensions compared to those that produce a measurable backscatter signal. When averaged over a sufficiently large number of locations in the tissues,  $\mu_b$  and  $\mu_t$  appear to be linearly related, which suggests that these coefficients reflect the properties of refractive inhomogeneities with a similar, albeit wide, range of dimensions.

† Changes in the mutual coherence of a beam incurred during its forward trip through a turbid medium can, in certain cases, be partially reversed during its return trip. However, the extent to which this occurs depends critically on the wave-structure function of the medium (Clifford and Wandzura 1981, Frehlich and Kavaya 1991).



## 5. Conclusions

The underlying scattering mechanisms that affect the signals acquired by OCT from tissues are manifold and complex. For tissues such as the artery with effective attenuation coefficients in the near infrared in the range  $30 < \mu_t < 100 \mu\text{m}$ , diffraction-limited imaging performance can only be achieved at optical depths,  $\mu_t z$ , at which single backscattering dominates. This limitation results from degradation of the mutual coherence of the probe beam by refractive inhomogeneities within the tissue that limit the focusing ability of the beam. Small-angle forward scattering can degrade the coherence of the beam without reducing its average intensity. In some tissues, imaging of structures at depths exceeding several hundreds of micrometres ( $\mu_t z > 5\text{--}10$ ) still appears to be feasible, provided that one recognizes and accounts for the trade-off between probing depth and imaging quality. The precise relationship between the magnitude of the measured OCT signals, however, and the properties of different types of tissue is not yet clear. This general problem will be the subject of future investigations.

## References

- Anderson R C and Browell E V 1972 First- and second-order backscattering from clouds illuminated by finite beams *Appl. Opt.* **11** 1345–51
- Born M and Wolf E 1983 *Principles of Optics* 6th edn (Oxford: Pergamon)
- Clivaz X, Marquis-Weible F, Salath R P, Novak R P and Gilgen H H 1992 High-resolution reflectometry in biological tissues *Opt. Lett.* **17** 4–6
- Clifford S F and Wandzura S 1981 Monostatic heterodyne lidar performance: the effect of the turbulent atmosphere *Appl. Opt.* **20** 514–16
- Fercher A F, Mengedocht K and Werner W 1988 Eye length measurement by interferometry with partially coherent light *Opt. Lett.* **13** 186–8
- Frehlich R and Kavaya M 1991 Coherent laser radar performance for general atmospheric refractive turbulence *Appl. Opt.* **30** 5325–52
- Hitzenberger C K 1991 Optical measurement of the axial eye length by laser doppler interferometry *Invest. Ophthalm. Vis. Sci.* **32** 616–24
- Huang D, Swanson E A, Lin C P, Schuman J S, Stinson W G, Chang W, Hee M R, Flotte T, Gregory K, Puliafito C A and Fujimoto J G 1991 Optical coherence tomography *Science* **254** 1178–81
- Ishimaru A 1978 *Wave Propagation and Scattering in Random Media* vol 1 (New York: Academic) ch 7
- Kazovsky L G and Kopeika N S 1983 Heterodyne detection through rain, snow, and turbid media: effective receiver size at optical through millimeter wavelengths *Appl. Opt.* **22** 706–10
- Lutomirski R F 1978 Atmospheric degradation of electrooptic system performance *Appl. Opt.* **17** 3915–21
- Parameswaran K, Rose K O and Krishna Murthy B V 1991 Relationship between backscattering and extinction coefficients of aerosols with application to turbid atmosphere *Appl. Opt.* **30** 3059–71
- Schmitt J M, Knüttel A and Bonner R F 1993a Measurement of optical properties of biological tissues by low-coherence reflectometry *Appl. Opt.* **32** 6032–42
- Schmitt J M, Knüttel A, Gandjbakhche A and Bonner R F 1993b Optical characterization of dense tissues using low-coherence interferometry *Proc. SPIE* **1889** 197–211
- Schmitt J M, Knüttel A, Yadlowsky M and Bonner R F 1993c Interferometric versus confocal techniques for imaging microstructures in turbid biological media *Proc. SPIE* **2135** 251–62
- Siegmán A E 1966 The antenna properties of optical heterodyne receivers *Appl. Opt.* **5** 1588–94
- Swanson E A, Izatt J A, Hee M R, Huang D, Lin C P, Schuman J S, Puliafito C A and Fujimoto J G 1994 In vivo retinal imaging by optical coherence tomography *Opt. Lett.* **17** 151–3
- Yura H T 1974 Optical heterodyne signal power obtained from finite sized sources of radiation *Appl. Opt.* **13** 150–7
- 1979 Signal-to-noise ratio of heterodyne lidar systems in the presence of atmospheric turbulence *Opt. Acta* **26** 627–44